Fusion and binary-decay mechanisms in the $^{35}Cl + ^{24}Mg$ system at $E/A \approx 8$ MeV

Sl. Cavallaro, E. De Filippo, G. Lanzanò, A. Pagano, and M. L. Sperduto
Dipartimento di Fisica dell'Università di Catania, LNS and INFN Catania, I-95129 Catania, Italy

R. Dayras, R. Legrain, and E. Pollacco
CEA, DAPNIA/SPhN CE-Saclay, F-91191 Gif-sur-Yvette Cedex, France

C. Beck, B. Djerroud,* R. M. Freeman, F. Haas, A. Hachem,† B. Heusch, D. Mahboub, A. Morsad‡ and R. Nouicer
Institut de Recherches Subatomiques IN2P3/Université Louis Pasteur, B. P. 28, F-67037 Strasbourg Cedex 2, France

S. J. Sanders
Department of Physics and Astronomy, The University of Kansas, Lawrence, Kansas 66045
(Received 6 March 1997; revised manuscript received 30 September 1997)

Compound-nucleus fusion and binary-reaction mechanisms have been investigated for the $^{35}Cl + ^{24}Mg$ system at an incident beam energy of $E_{lab} = 282$ MeV. Charge distributions, inclusive energy spectra, and angular distributions have been obtained for the evaporation residues and the binary fragments. Angle-integrated cross sections have been determined for evaporation residues from both the complete and incomplete fusion mechanisms. Energy spectra for binary fragment channels near the entrance-channel mass partition are characterized by an inelastic contribution that is in addition to a fully energy damped component. The fully damped component which is observed in all the binary mass channels can be associated with decay times that are comparable to, or longer than, the rotation period. The observed mass-dependent cross sections for the fully damped component are well reproduced by the fission transition-state model, suggesting a fusion followed by fission origin. The present data cannot, however, rule out the possibility that a long-lived orbiting mechanism accounts for part or all of this yield. [S0556-2813(98)02302-4]

PACS number(s): 25.70.−z

I. INTRODUCTION

In recent years heavy-ion induced reactions, involving intermediate mass systems as light as $A_{CN} \leqslant 60$ at bombarding energies $\leqslant 10$ MeV/nucleon, have been studied for various target+projectile combinations over a wide energy range [1–8]. Near the Coulomb barrier (region I), the complete fusion (CF) process is the dominant reaction mechanism. At higher energies (region II), however, this process is limited by the contributions of other, competing processes such as quasielastic and deep-inelastic collisions (DIC). The CF cross section is still increasing with energy, but at a much slower rate than in region I. At even higher energies (region III) the general instability of the composite system leads to a decreasing CF cross section with increasing beam energy. Strong competition between fusion and other damped mechanisms characterize regions II and III. The present measurement, which has been performed at an incident energy corresponding to region III for the complete-fusion cross sections, is designed to further study the competing reaction mechanisms at higher energies. Several competing mechanisms have been suggested to absorb the reaction flux in regions II and III. Heavy-ion resonances and orbiting mechanisms have been shown to compete with fusion for the incident flux in region II [9], at least in some systems.

In the incomplete fusion process (ICF) only part of the entrance channel mass is incorporated into the resulting compound system. While this process is insignificant at lower energies [10,11], it can quickly rise at higher energies in region III, leading to a large reduction of the complete fusion cross section [10].

Classical trajectory models that include consideration of frictional forces and the effects of thermal fluctuations, can be used to predict observables such as the mean values and widths of the mass, charge and energy flow in damped, deep-inelastic collisions [12,13]. By the Langevin method (LM), and on the basis of the surface friction model of Ref. [14], for instance, it is further possible to model the competition between fusion and DIC mechanisms by introducing temperature-dependent coefficients for the radial, tangential and deformation friction contributions, respectively. However, the determination of these coefficients to the precision needed to reproduce the fluctuations around dynamical central values has only been accomplished for a few cases. More experiments are needed where the excitation functions for fusion and DIC are measured simultaneously for a given nuclear system.

The present measurement is part of a more general experimental program devoted to the study of the limits of compound nucleus formation by measuring the macroscopic observables related to the formation and decay of a single nuclear system through several different entrance channels.

*Also at Department of Chemistry, University of Rochester, Rochester, New York 14627.

†Permanent address: Faculté des Sciences, Université de Nice, F-06034 Nice, France.

‡Permanent address: Faculté des Sciences, Université Hassan II, Casablanca, Maroc.

Within the LM method a limit is reached when a given trajectory starts to be captured in the pocket of the ion-ion potential. At this point there is no further information that can be determined for the dynamical trajectories [15,16], and the two interacting nuclei can be thought to form a dinuclear system (DNC), from which they can either fuse into a fully equilibrated compound nucleus (CN), or escape from the ion-ion potential well, producing a damped orbiting process.

The decay properties of the binary fragments produced as a consequence of the fission after fusion [17] or after scission of a long-lived orbiting dinuclear system [18] have been described in the literature on the basis of the phase-space configurations at the saddle point of the intermediate system. It has been found to be difficult to experimentally distinguish between the fission and orbiting mechanisms as both are expected to give very similar behavior [19]. A fusion-fission origin has been suggested for fully damped yields associated with reactions populating the ^{56}Ni [1], ^{58}Ni [2], and ^{47}V [3] compound nuclei. On the other hand, similar binary yields observed for certain lighter systems have been alternatively explained in terms of a statistical dinucleus orbiting model [4–6].

This paper reports on the results of both the fusion-evaporation and binary fragment (fusion-fission and DIC) cross sections for the ^{35}Cl+^{24}Mg reaction at E_{lab}=282 MeV, obtained by inclusive energy and angular distribution measurements as functions of the nuclear charge of the detected fragments. Previously, this reaction has been studied only at lower energies [20] and only a few results have been published [21]. However, the composite system reached by this reaction ^{59}Cu has been extensively investigated in fusion regions II and III by the ^{19}F+^{40}Ca [22] and ^{32}S+^{27}Al reactions [22–27]. These previous measurements have shown pronounced entrance-channel effects for the relative contributions of DIC and the ICF process. However, fission yield measurements were lacking. It is then also interesting to study the formation of the same ^{59}Cu nucleus in conditions of an intermediate entrance-channel mass asymmetry.

Complementary information concerning the mean excitation energies and average angular momenta of binary-fragments from the ^{59}Cu intermediate system formed by the ^{35}Cl+^{24}Mg reaction will be reported in a forthcoming paper based on in- and out-of-plane angular correlations between light particles and heavy fragments [28].

In the next section, the experimental procedure is described. In Sec. III, the fusion-evaporation yields are given and discussed. The properties of the binary fragments are presented in Sec. IV. In Sec. V, the compound-nucleus-decay models used to discuss the data are briefly introduced, and comparisons of the binary fragment experimental results with the predictions from the fission transition-state model are presented. In Sec. VI, the present data are discussed in the context of previously reported results and used to explore how different competing mechanisms lead to limitations in the formation of the ^{59}Cu compound nucleus. Finally, a summary of the main results and conclusions are given in Sec. VII. A recent paper has presented the preliminary results obtained from the fragment-fragment angular correlation measurements performed at E_{lab}=278.4 MeV [29], which confirm well the main conclusions of this work and provides some information on the possible occurrence of three-body breakup processes.

II. EXPERIMENTAL PROCEDURE

The experiment was performed by the Saclay Post-Accelerator Tandem Facility. A ^{35}Cl pulsed beam (charge state $Z=14^{+}$) accelerated to an energy E_{lab}=282.4 MeV was focussed onto a self-supporting rolled ^{24}Mg target, located in a 2 m diameter scattering chamber. The ^{24}Mg foils, of 99.9% isotopic enrichment, had areal densities of 350 ± 32 and 255 ± 20 μg/cm^2, respectively. The time structure of the pulsed beam had a period of 37 ns. The beam current was varied from a few nA to $\approx$20 nA, depending on the positions of the detectors and the corresponding counting rates. Carbon and oxygen contaminants were experimentally estimated at $\leqslant$10 μg/cm^2 each, using a 2 MeV α-beam backscattering technique. Heavy fragments (Z=13–26) were detected by a Bragg-curve ionization chamber (BIC) filled with CF4 gas at a pressure of 150 Torr in the 3° to 12° angular range with a 1° step increment. Four small gas-ionization chambers, at a pressure of 51 Torr of CF4 gas, followed by silicon E detectors, were used to detect fragments with Z=3 to Z=26 in the 10°–90° angular range with a 2° step. An additional gas-silicon telescope was located at a fixed position, 10° with respect to the beam as a monitor. The beam current was measured in a Faraday cup and integrated. To correct for carbon contamination, measurements were also made at the same detector angles and with comparable beam conditions using a 100 μg/cm^2 thick, self-supporting, carbon foil as a target [30]. Absolute cross sections were determined by measuring the elastic scattering of 282.4 ^{35}Cl ions from the ^{24}Mg target at θ_{lab}=3°–16° and comparing with the elastic scattering predictions. The optical model analysis of the experimental data performed with the code PTOLEMY is shown in Fig. 1. This calculation was made using the parameters V_R =5.1 MeV, r_R=1.46 fm, a_R=0.5 fm, W_I=9.3 MeV, r_I =1.3 fm, a_I=0.42 fm for the real and imaginary parts of the potential, respectively, and a Coulomb radius parameter r_C =1.2 fm. These parameter values have been extrapolated from the low-energy data of Ref. [31].

Taking into account the uncertainties associated with all of the measured parameters, a global error of 17% is attributed to the absolute values of the differential cross sections reported in this paper. Double differential cross sections determined from the experiment have been corrected for the contribution of the carbon contaminant by subtracting from the measured cross sections the component

$$\left(\frac{d^2\sigma}{d\Theta dE}\right)_{\rm corr}=\left(\frac{d^2\sigma}{d\Theta dE}\right)_C\frac{t_{\rm cont}}{t_{\rm carb}},\qquad(1)$$

where $(d^2\sigma/d\Theta dE)_C$ is the cross section determined for the reaction ^{35}Cl+^{12}C [30], $t_{\rm carb}$ is the carbon-target thickness and $t_{\rm cont}$, the carbon contamination on the ^{24}Mg target. These corrections are generally $\leqslant$10%. However, because of their very different kinematics, reactions induced on the carbon contaminant can contribute significantly to the yield of some fragments at particular angles and energy ranges. The energy calibrations of the BIC detector and of the gas-silicon telescopes were determined by measuring the peak positions

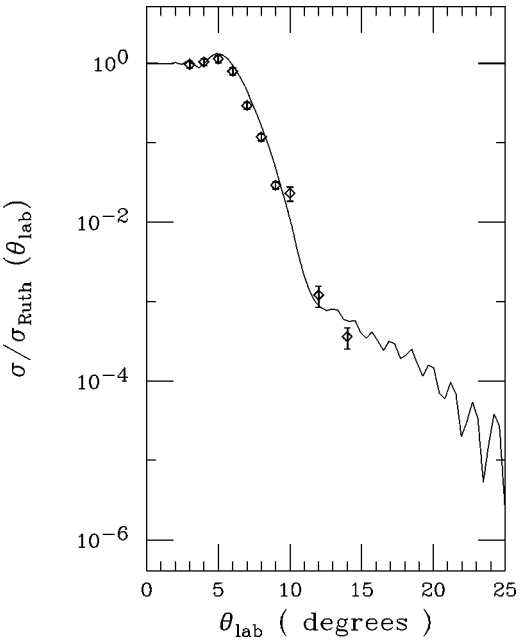

FIG. 1. Comparison of the experimental angular distribution for elastic scattering to Rutherford contribution, to optical model predictions. Experimental values are indicated by diamond symbols. Calculations have been performed with the code PTOLEMY.

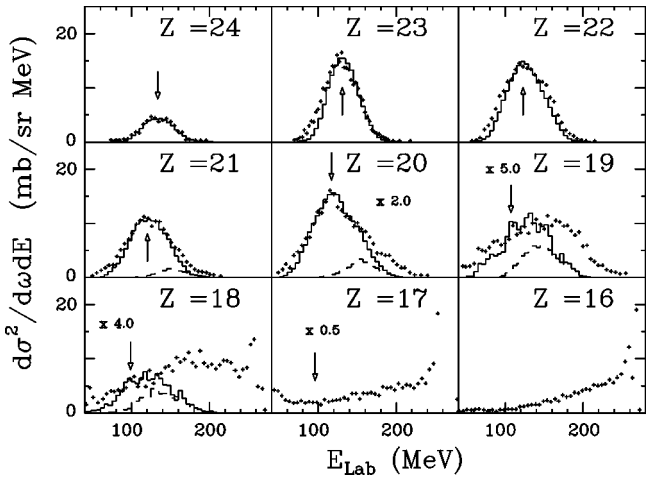

FIG. 2. Energy spectra of fragments with $Z=24$–16, measured at $\theta_{\rm lab}=7°$. To provide a more sensitive view of the results, data size for $Z=20$, 19, 18 and $Z=17$ have been scaled by the factors indicated in the figure. The arrow positions indicate the expected centroid values from Eq. (3). ER spectra (CF+ICF contributions) calculated by the LILITA statistical-model code are indicated by the full-line histograms for fragments with $Z=24$ to $Z=18$; The ICF component is indicated by the dashed-histograms for fragments with $Z=21$ to $Z=18$.

of the elastically scattered ^{35}Cl nuclei from a 400 μg/cm^2 thick, gold target and using the known kinematics for this reaction. In the energy calibration procedure, corrections for energy losses in the ^{24}Mg target (in the half-thickness approximation and with exception of heaviest residues, see later), and for energy losses of the fragments passing through the Mylar windows of the BIC and the IC were included. Pulse-height-defect corrections for the Si detectors were taken into account using the procedure given in [32].

III. FUSION-EVAPORATION CROSS SECTIONS

The dominant mechanism by which the compound system deexcites in this reaction, at least for lower spin values, is through the emission of light particles. Cross sections for the evaporation residues arising from both the complete fusion and possibly by incomplete fusion processes were therefore determined. Energy spectra obtained at $\theta_{\rm lab}=7°$ are shown in Fig. 2. The bell-shaped patterns characteristic of evaporation residues can be seen for $Z=24$ to $Z=21$ fragments. These data are compared to statistical-model calculations with the code LILITA [33].

In making the comparison with model calculations it is important to account for fragment energy losses in the target. For the heavier fragments these losses can amount to 7 MeV, as compared to a ^{35}Cl incident beam energy loss of only 2.6 MeV. The calculated spectra in Fig. 2 were obtained by considering the reaction as occurring in a stack of twenty thin-''targets'' with a total thickness equivalent to the actual ^{24}Mg target used in the experiment. The LILITA spectra were calculated for each of the twenty ''targets'' and then corrected for the energy loss through the remaining targets. The final, ''degraded'' LILITA spectrum was then obtained by a convolution of the twenty constituent spectra. This procedure allows one to compare the experimental Z-residue spectra with those expected from the full momentum transfer kinematics.

For complete fusion events, the light particles are emitted in the rest frame of the recoiling nucleus, with angular distributions symmetric around 90° and with Maxwellian energy spectra. If, in addition, the angular distributions are assumed to be isotropic, then the energy spectra of the evaporating residues can be expressed by [33]

$$\left(\frac{d^2\sigma}{d\Omega dE_{ER}}\right)=\frac{K(2E_{ER})^{1/2}}{M_{ER}^{3/2}} \times e^{-E_{CN}\sin^2\theta_{\rm lab}/s^2M_{CN}}e^{-(E_{ER}^{1/2}-E_C^{1/2})^2/s^2M_{CN}}, \tag{2}$$

where E_{ER} and M_{ER} are the kinetic energy and the mass of the evaporating fragment, respectively, E_{CN} is the kinetic energy of the compound system, K is a normalization factor, and s is the standard deviation parameter of the Gaussian velocity distribution of the recoiling residues. For M_{ER}, the mean values of isotope mass-distributions calculated by LILITA, have been assumed.

The E_C term is given by

$$E_C=\frac{M_{ER}E_{CN}}{M_{CN}}\cos^2\theta_{\rm lab}. \tag{3}$$

If the E_{ER} energies are large compared with the s^2M_{CN} term, then the energy variation resulting from the $E_{ER}^{1/2}$ term can be neglected compared to that arising from the exponential term and the resulting energy spectra predicted by Eq. (2) are centered at the energies given by Eq. (3). The experimental observation of energy spectra centered at these energies is then a signature of full momentum transfer. Equations (2) and (3) are no longer exact if the angular distributions of

evaporated particles are anisotropic, however departures from Eq. (2) are expected to be relatively small, especially in reverse kinematics conditions. In the present case, the Eq. (3) values are found to be lower than residue energy spectrum centroids calculated by the LILITA code with anisotropic angular distributions by only 1 to 1.5 %. Then, for the present reaction, the centroid energies obtained using Eq. (3) are a good measure of the extent to which incomplete momentum-transfer processes occur.

In Fig. 2, the predicted centroids from Eq. (3) are shown by arrows. The excellent agreement with the observed centroids indicates that there is no appreciable contribution of incomplete fusion processes for fragments with $22 \leqslant Z \leqslant 24$. For instance, if a preequilibrium α particle was ''lost'' in the reaction by either the projectile or target before the fusion process occurs, centroid energy shifts of ≈ -14 or ≈ 10 MeV, respectively, would be expected. Since no shift was found, these fragment yields have been ascribed to the complete fusion mechanism. It should also be noted that the LILITA calculations reproduce quite well both the energy centroid and the shape of the experimental spectra for these fragments. This justifies using these calculations to discriminate between the complete fusion process and other reaction mechanisms.

A departure from the bell-shaped behavior is clearly seen for the fragments with $Z=20$ and, to a lesser extent, also for $Z=21$. The deviation from the compound-nucleus evaporation behavior becomes very large for fragments with $Z \leqslant 19$, indicating that faster mechanisms other than complete fusion are contributing to these yields (see below): quasielastic and deep-inelastic processes.

Evaporation-residue cross sections of complete fusion were generally determined for fragments with $Z>21$, by integration of experimental angular spectra. For $\theta_{\rm lab}<3°$, and only in a few cases where identification thresholds prevented the use of experimental data (as at most forward angles for $Z=24$), LILITA calculations were used to extrapolate the angular distribution after normalization to the experimental data at a larger angle.

To better fit the energy spectra of $18 \leqslant Z \leqslant 21$ residues, at least at the most forward angles, it was necessary to introduce a contribution from an incomplete fusion process characterized by a loss of mass of ≈ 8 amu from the target. This effect was simulated by calculating evaporation-residue spectra from the reaction ^{35}Cl+^{16}O using the LILITA code and assuming a critical angular momentum of $28\hbar$. For those spectra where a centroid shift was evident, the heights of both the complete- and incomplete-fusion components were adjusted simultaneously in order to obtain the best overall reproduction of the data. The decompositions in the CF and ICF contributions are shown in Fig. 2 and also in Fig. 3 for $Z=20$ residues detected at four different angles. For $Z=19$ and $Z=18$ residues the presence of deep-inelastic components increased the difficulty of separating the various reaction components.

Experimental angular distributions including all mechanism contributions are shown in Fig. 4 for fragments with $16 \leqslant Z \leqslant 24$. For $Z=22$ to $Z=24$ residues, total yields are attributed to the CF process and compared with LILITA calculations. For residues with $Z=18$ to $Z=21$, contributions from the CF and ICF processes have been separated. For the

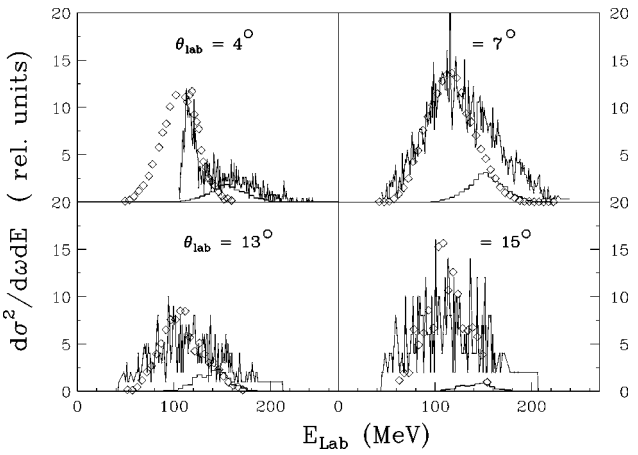

FIG. 3. Energy spectra of $Z=20$ fragments , measured at $\theta_{\rm lab}=4°$, 7°, 13°, and 15°, respectively. The $\theta_{\rm lab}=4°$ spectrum exhibits a large energy threshold due to the identification energy-limit of the Bragg detector used for most forward angles. Diamond symbols and histograms indicate the CF and the ICF contributions, respectively.

$Z=18$ and 19 fragments, are reported both the experimental total yields, and the ''extracted'' CF and ICF contributions. For the projectilelike $Z=16$ and 17 fragments, the spectra become dominated by quasielastic and deep-inelastic scattering contributions.

Evaporation-residue cross sections from complete fusion were determined by integration of associated angular distributions. In few cases where identification thresholds at the most forwards angles prevented the use of the experimental data, LILITA calculations, after normalization to the experimental data at a larger angles, were used to extrapolate the angular distributions down to 0°. Evaporation residues from incomplete fusion were determined in the same manner. The complete fusion-evaporation cross section amounts to 600 $\pm$105 mb, whereas the incomplete fusion evaporation amounts to 60$\pm$30 mb. Thus, the total evaporation residue cross section is found to be 660$\pm$110 mb.

The complete-fusion evaporation-residue cross sections, obtained by integrating the angular distributions for the different charge channels, after subtraction of the estimated ICF contribution, are shown in Fig. 5 by the full circles. Compared to these experimental results are cross sections calculated using the LILITA and CASCADE [34] codes.[1] For these calculations, the diffuse cutoff approximation was assumed for the entrance-channel transmission coefficients [34], taking the critical angular momentum for fusion as $l_{\rm cr}= 38\hbar$ and a diffuseness of $\Delta = 1\hbar$, extracted from the total measured fusion-evaporation cross section. Known low-lying states were used to determine the fragment level densities at low excitation energy. As seen in the figure, both calculations show an upward shift in Z values of $\Delta Z \approx 2$ with respect to experimental values. It has been suggested that this shift may be due, to some extent, to the effects of deformation in the evaporating system (see, i.e., Refs. [23,35]).

Taking deformation into account, however, represents a

[1]See [20], and references therein for light-particle optical potential and level density parameters.

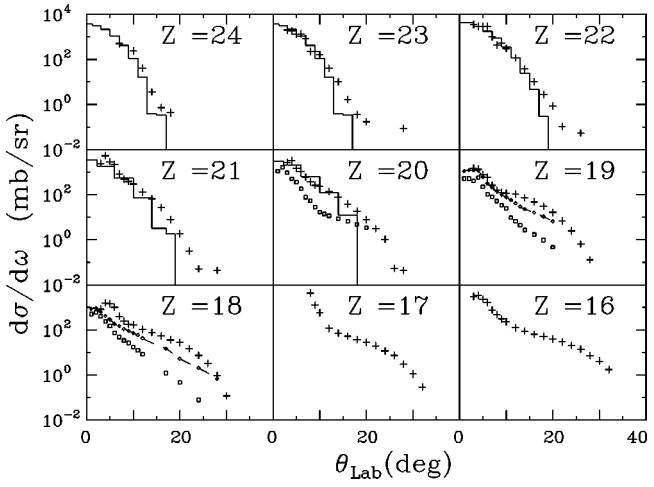

FIG. 4. Angular distributions of fragments with $Z=24$ to $Z=16$. The plus symbols are experimental data including all contributions. For fragments with $Z=24$ to $Z=22$ total yields are attributed to the CF process and are compared with the corresponding LILITA calculations (histograms). For fragments with $Z=21$ and $Z=20$ the experimental yields are attributed to the fusion processes (CF+ICF). For $Z=19$ and $Z=18$ the fusion contributions have been extracted from total yields as indicated by diamond symbols joined by dashed lines. For fragments with $Z=21$ to $Z=18$ the ICF contributions are shown by squared symbols.

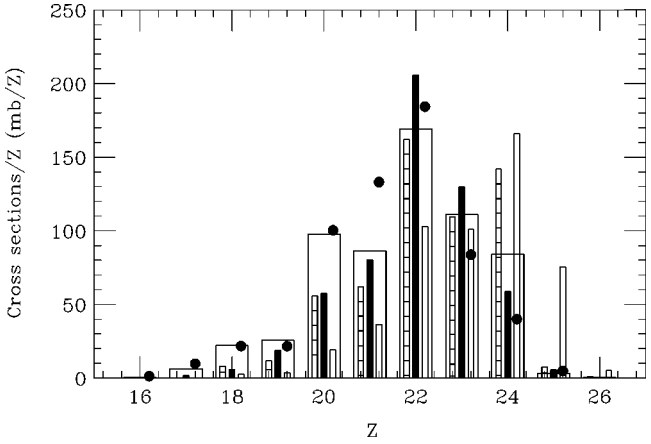

FIG. 5. Comparison between the experimental complete fusion-evaporation elemental distributions (full circles) and the predictions of the LILITA and CASCADE statistical-model codes. Empty histograms are for LILITA: small width for standard parameter calculations [33]; large width, when ''deformation'' of evaporating nuclei is taken into account. Similarly for the CASCADE code: hatched histograms for standard calculations [34], and full-histograms with ''deformation'' effects, respectively.

difficult task. Different procedures have been debated in the literature in connection with fitting of proton and α spectra [36–41]. Due to the lack of experimental transmission coefficients for emission of light particles from hot deformed nuclei and limitations of available multistep evaporating code for deformed nuclei, this problem is still open and the object of investigations [42,43].

A simple, although schematic, way of taking into account deformation effects is to increase the potential radius in calculating the transmission coefficients for deformed nuclei and also to increase the moment of inertia radius parameters used in determining the available phase space for light fragment decay. This procedure has been used in the present analysis in order to take into account deformation effects; as a matter of fact the deformation could, in our case, simulate a similar effect as the ICF mechanism in the residue charge distribution.

Data reported in literature for this mass region and lower excitation energy [36], indicate the need to increase the potential radius r by 10 to 25 % and to introduce an angular momentum dependent yrast line in the fitting procedure of evaporation spectra, with a moment of inertia given by $I=I_0(1+\mathrm{def}J^2+\mathrm{defs}J^4)$. The ranges for the related parameters are about $r_{0\ \mathrm{LDM}}=1.15$ to 1.28, def=1 to 3.2×10^{-4} and defs=0 to 20×10^{-8}, respectively. Based on the results obtained at higher excitation energy for the same ^{59}Cu nucleus by fragment-light particle coincidence measurements [28], $r=r_0 1.10$ and $r_{0\ \mathrm{LDM}}=1.28$ and def$=3.2\times10^{-4}$ and defs$=16\times10^{-8}$ have been here assumed in the CASCADE calculations and $r=r_0 1.10$ and $r_{0\ \mathrm{LDM}}=1.28$ in the LILITA calculations. The resulting charge distributions are shown in Fig. 5, indicating a better agreement between data and theoretical calculations.

Figure 6 reports the evaporation-residue Z distributions for the ICF contributions together with corresponding LILITA calculations. When performing these statistical model calculations, a total ICF cross section of $\sigma=60$ mb was assumed.

IV. BINARY FRAGMENTS

For fragments such that $(3\leqslant Z\leqslant 17)$, the energy spectra are no longer consistent with the behavior expected for heavy residues arising from a fusion-evaporation process. These nuclei are mainly the remnants of quasiprojectile or quasitarget fragments from binary reactions. They may also result in part from a fusion-fission process as we will show later. In this case, the corresponding cross section should be added to the fusion cross section.

Figure 7 shows the double differential cross section $(d^2\sigma/d\Theta_{\mathrm{c.m.}}dE_{\mathrm{c.m.}})$ contours, as a function of total kinetic energy (TKE) and angle $\Theta_{\mathrm{c.m.}}$ in the center-of-mass system, for $5\leqslant Z\leqslant 16$ fragments. The data exhibit a large range of kinetic energies and angular distributions which are strongly depending on both energy and fragment Z value. The angular

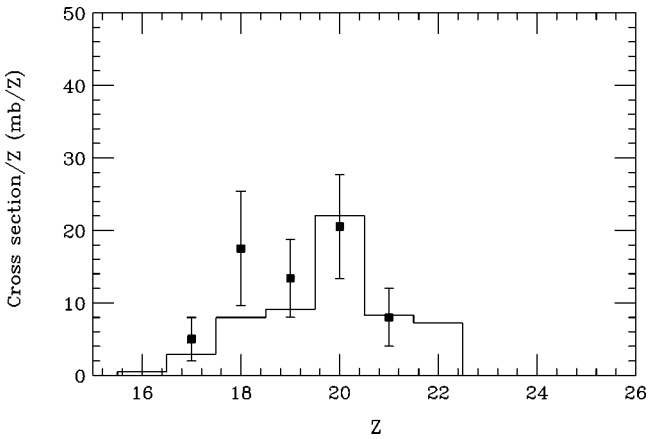

FIG. 6. Comparisons between the ICF experimental data (full squares) and LILITA code calculations.

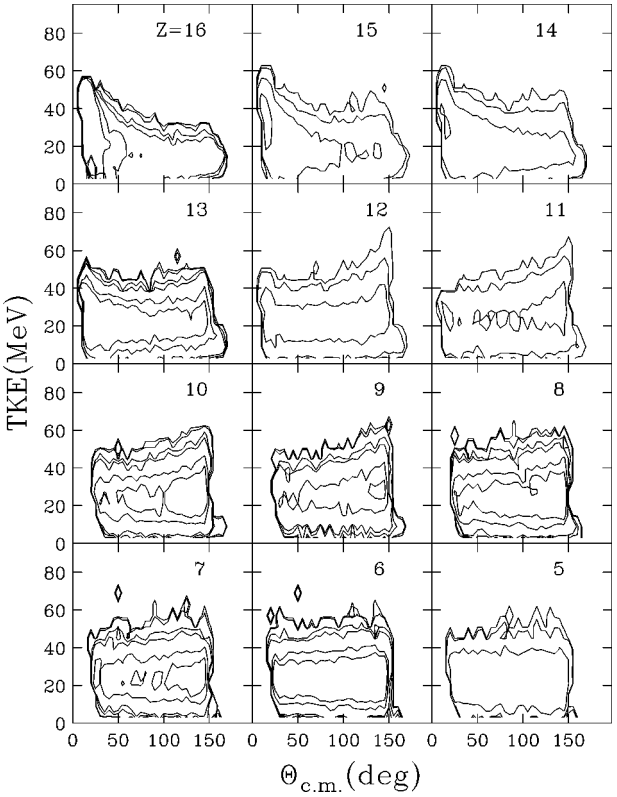

FIG. 7. Contour plots of double differential cross sections versus TKE and $\Theta_{c.m.}$ for fragments with Z=16 to Z=5.

distributions show generally an initial $(d^2\sigma/d\Theta_{c.m.}dE_{c.m.})$ constancy at low energy, which is progressively lost at higher energies. In order to extract more detailed information, each map has been divided in 5-MeV wide energy slices and separate angular distributions generated for each slice. In some cases a single component dominates the entire kinetic energy range. This is seen in Fig. 8 for the light fragments with $Z=3$ to 5. In this figure the contributions of all energy slices have been summed. One finds for the lightest fragments that the kinetic energies are fully damped and

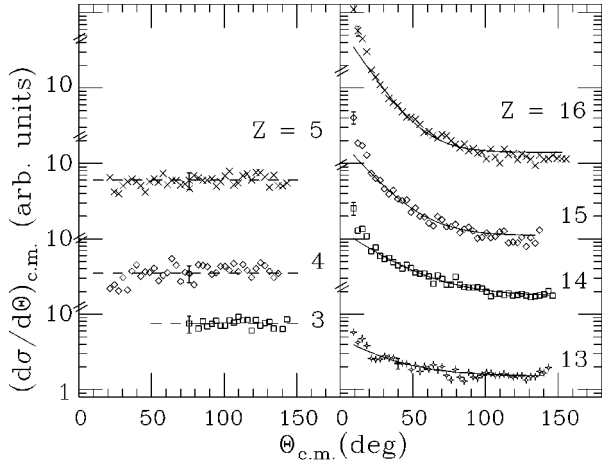

FIG. 8. Angular distributions $d\sigma/d\Theta_{c.m.}$ for fragments with $Z=3,4$ and $Z=5$, (left side); and $Z=13$, 14, 15, and 16, (right side), as a function of $\Theta_{c.m.}$. For $Z=13$ to $Z=16$ and $\Theta_{c.m.}\leqslant 18.5°$ (grazing value), data are mainly due to the positive angle (near-side) contributions. Curves are fits to the data as described in the text.

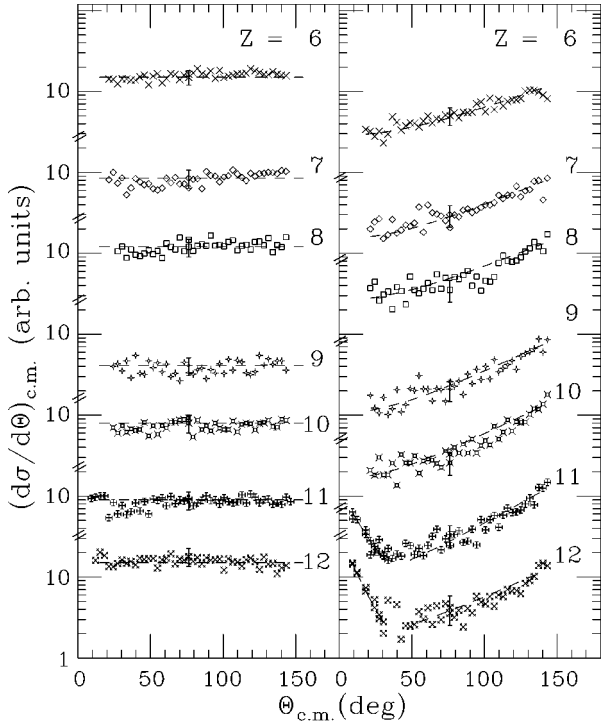

FIG. 9. The same as in Fig. 8, for $Z=6$ to $Z=12$. The fully and the partially damped components are reported on the left and right sides, respectively. Energies up to 25–30 MeV have been considered for fully damped components and energies from 25–30 MeV up to the largest energies for the partially damped ones.

the angular distributions are almost flat. For fragments with $Z=13$ to 16, a forward-peaked and partially damped component (projectilelike component) is present together with a second, angle independent component. The former becomes very small at energies higher than ≈ 29 MeV. For fragments with $Z=6$ to 12, as shown in Fig. 9, a component with a constant cross section can be seen up to 25–30 MeV (left side of figure), whereas for higher energies, anisotropic components are also present. For $Z=6$ to $Z=10$, the anisotropic components are backward peaked (targetlike component). For fragments with $Z=11$ and $Z=12$, both projectilelike and targetlike components are present, indicating a net transfer of nucleons from both target to projectile and vice versa.

The energy dependence of the angular distributions clearly indicate different reaction times, not only for different fragment pairs, but also for same pair at different net energy loss. The decay time estimates for a surface reaction can be deduced from the angular distribution analysis using a simple Regge-Pole model described in Ref. [44]. This analysis leads, however, to almost flat distributions for decay times comparable to the rotation time of the dinuclear system. In cases where there are both long- and short-lived reaction components, the Regge model can be modified by the addition of a constant term h to account for the long-lived component:

$$\frac{d\sigma}{d\Theta_{c.m.}} = k[e^{-\Theta_{c.m.}/\omega\tau} + e^{-(2\pi-\Theta_{c.m.})/\omega\tau}] + h. \qquad (4)$$

Here, ω is the rotational frequency and τ is the decay time of the dinuclear system. The rotational energy and the angular

TABLE I. Binary fragment cross sections and average c.m. kinetic energies, for both (a) fully damped and (b) partially damped, components. Cross section values are obtained by integration of angular distributions reported in Figs. 8 and 9. The kinetic energies, TKE values, are given in MeV. The decay times τ_1 and τ_2 are reported in units of the rotation time $T \approx 1.6\times10^{-21}$ s (see text).

Z	σ_a (mb)	σ_b (mb)	$(TKE)_{(a)}$	$(TKE)_{(b)}$	τ_1/T	τ_2/T
3	7.2±1.5		15.5±2			
4	5.9±0.9		20.0±2			
5	9.7±3.0		22.5±2			
6	26.9±4.4	10.4±1.8	21.0±2	28±2		$0.19\pm^{0.02}_{0.02}$
7	14.3±2.5	7.0±1.2	22.0±2	32±2		$0.16\pm^{0.02}_{0.02}$
8	17.2±3.2	9.3±1.6	22.0±2	31±3		$0.14\pm^{0.02}_{0.02}$
9	8.5±1.4	5.2±0.9	22.0±2	31±3		$0.12\pm^{0.02}_{0.02}$
10	15.2±1.8	8.5±1.4	22.0±2	31±3		$0.10\pm^{0.01}_{0.02}$
11	14.1±2.5	7.6±1.3	24.0±2	33±2	$0.04\pm^{0.02}_{0.01}$	$0.07\pm^{0.01}_{0.02}$
12	26.6±4.8	10.0±1.5	22.0±2	33±2	$0.03\pm^{0.02}_{0.01}$	$0.07\pm^{0.01}_{0.03}$
13	8.8±1.8	26.6±4.2	22.0±2	30±2	$0.08\pm^{0.02}_{0.02}$	
14	14.0±2.8	61.3±12.0	21.0±2	28±2	$0.08\pm^{0.02}_{0.01}$	
15	8.0±1.6	57.6±10.0	19.0±2	40±3	$0.05\pm^{0.02}_{0.01}$	
16	20.0±4.0	130.0±20.0	15.5±2	45±4	$0.04\pm^{0.02}_{0.01}$	

momentum at the scission configuration which are related to ω, can be estimated following the procedure discussed in Ref. [45].

The rotation time of the dinuclear system $T=2\pi/\omega$ was found to be $\approx 1.6\times10^{-21}$ s. Fits of angular distributions by Eq. (4) are reported in Table I. The τ_1 parameter refers to the decay time of the forward-peaked component. To obtain the τ_2 decay time of the backward-peaked component (targetlike behavior), the Θ abscissa has been changed in $\Theta_2=\pi-\Theta$. In the fitting procedure, the fully damped part of spectra of all fragments was successfully fitted with only a component with $d\sigma/d\Theta_{c.m.}=$const, whereas the partially damped components, with TKE$\geqslant$29 MeV and fragments with $Z=6$ to 17 were fitted with Eq. (4). In these cases, the cross sections corresponding to the constant term in Eq. (4) accounted for only a few percent of the total yields. Table I reports the angle-integrated cross section and kinetic energy values for both fully damped components and partially damped components for fragments with $Z=3$ to $Z=16$.

Figure 10, presents the total measured yields for fragments with $Z=3$ to $Z=25$, the dashed-line histograms correspond to the fully damped cross sections for $Z=3$ to $Z=17$ fragments obtained by extrapolating the experimental distribution over the complete angular range. For the sake of completeness, the figure also shows the contribution from the complete-fusion process (full line histogram). The excess yield around $Z=16$–17 can be imputed to quasielastic and partially damped processes.

V. TRANSITION-STATE CALCULATIONS

Although neutron, proton, and α-particle emissions are the dominant particle-decay modes for compound nuclei as formed in the fusion reactions of low-mass systems, binary fission is also a possible process [17]. For lighter systems that are below the Businaro-Gallone limit, the fission barriers are such as to favor the breakup of the compound nucleus into asymmetric-mass channels. For these systems, light-particle emissions can be thought of as one extreme of the fission mass distribution [46]. Fission to the more symmetric-mass binary channels tends to be restricted in these systems to partial waves near to the critical angular momentum for fusion l_{cr}. Calculations using the transition-state model, where the fission decay width is determined by the density of states at the saddle point, have been found to successfully reproduce the observed fission cross sections in system of mass $A\approx100$ [47] and lighter [17], when the saddle-point energy is calculated for different mass asymmetries and spins using the finite-range model (see, e.g., Ref. [48]). Binary fragment production is also predicted by the extended Hauser-Feshbach method (EHFM) [49], where the partial decay widths are determined by the available phase space at the scission, rather than the saddle, configuration. This method has been successfully used to explain the yields

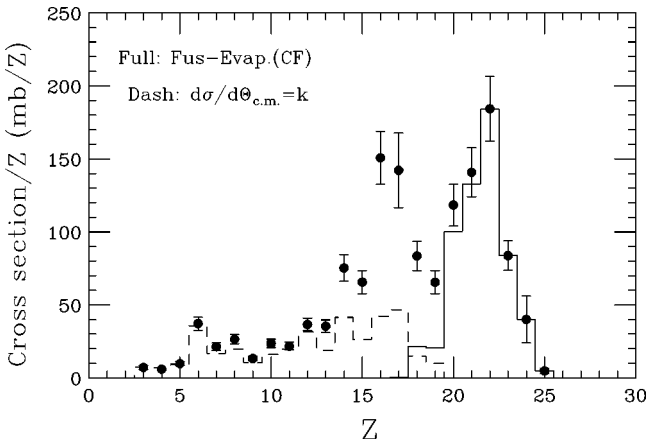

FIG. 10. Measured total Z distribution (full circles). For $Z=3$ to $Z=17$, the dashed line histogram is the contribution of the fully damped component obtained by integration of the isotropic component of $d\sigma/d\Theta_{c.m.}$. The full-line histogram represents the experimental complete fusion-evaporation Z distribution. The excess yield observed around $Z=16$ is due to important contribution from quasielastic or partially damped collisions (see text).

of both evaporation residues and intermediate mass fragments, as well as the kinetic energies of the heavier fragments.

Since the saddle-point shape in this mass region corresponds to having two touching spheroids in an elongated configuration, any process that leads to the formation of a long-lived, dinuclear orbiting system of similar deformation is likely to result in angular and excitation energy distributions that are indistinguishable from those of a fusion-fission mechanism. The most unambiguous way to distinguish between the fusion-fission and long-lived orbiting mechanisms in light systems is to establish an entrance channel dependence of the fully energy-damped yields that cannot be accounted for by differences in the expected compound-nucleus spin distribution. Such studies have not been done for the present system. Based on the number of open channels systematics of Beck *et al.* [9], however, a significant orbiting yield is not expected for the present reaction and consequently, in the following we will assume a fusion-fission origin for these yields.

In the present analysis, the formulation of Ref. [17], with its basic-parameter values, is used to calculate the mass-dependent yields and kinetic energies for the fission fragments. This calculation uses the spin and mass-asymmetry-dependent saddle-point energies of the finite-range model [48] to determine the transition-point phase space.

In light systems the saddle- and scission-point configurations are believed to be similar. Therefore, the geometry of the two fragments at scission is based on the calculated saddle-point configuration of the finite-range model.

The total kinetic energy in the exit channel is assumed to be

$$T_{KE}=V_C+V_N+\frac{\hbar^2 L_{\rm out}(L_{\rm out}+1)}{2\,{\rm Im}_{\rm rel}}$$

with

$$L_{\rm out}=\frac{{\rm Im}_{\rm rel}}{{\rm Im}_{\rm tot}}J_{\rm tot}$$

and

$${\rm Im}_{\rm tot}={\rm Im}_{\rm rel}+{\rm Im}_3+{\rm Im}_4,$$

where V_C and V_N are the Coulomb and nuclear energies, respectively. $\mathrm{Im}_{\rm rel}$ is the relative moment of inertia and Im_3 and Im_4 are the moment of inertia of fragments 3 and 4, respectively.

The diffuse cutoff model [34] was used to determine the fusion partial cross section distribution, with the diffuseness and critical angular momentum for fusion taken as $\Delta=1\hbar$ and $l_{\rm cr}=38\hbar$, respectively, as assumed for the evaporation residue analysis presented earlier. The ratio of the fission decay width Γ_f to the total decay width of the compound nucleus, $\Gamma_{\rm tot}$, was determined using the statistical model, with

$$\Gamma_{\rm tot}=\Gamma_n+\Gamma_\alpha+\Gamma_p+\Gamma_f,$$

and

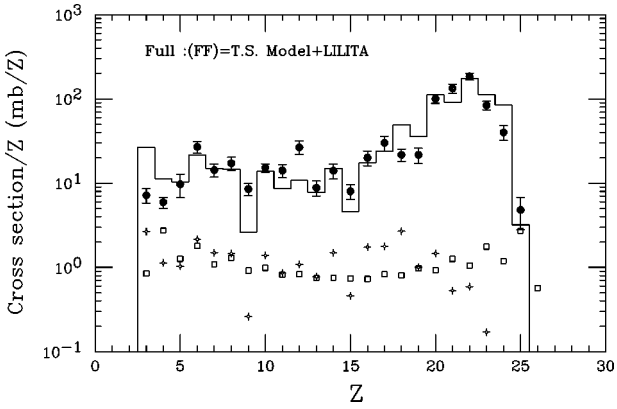

FIG. 11. Measured elemental distribution (full circles) for CF and completely damped processes. The open squares (scaled down by a factor 0.1) are the fission yields predicted by the FF model before evaporation. The crosses are the fission yields (also scaled down by a factor of 0.1) after evaporation (using the code LILITA). The calculated Z distribution for evaporation residue (as given by LILITA) and fission fragments (as given by the FF model after evaporation) is shown by the full line histogram in very good agreement with the data.

$$\Gamma_f=\sum_{A_L=6}^{A_{CN}/2}\ \sum_{Z_L=A_L/2-2}^{A_{CN}/2+2}\Gamma_f(Z_L,A_L), \tag{5}$$

where $\Gamma_f(A_L,Z_L)$ is the decay width for the channel specified by the lighter fragment of charge Z_L and mass A_L. The branching ratios and fission cross sections are calculated using energy-integrated widths for compound-nucleus decay. (See Ref. [17] for a more complete discussion).

Since it is possible that fission events will leave the resulting fragments at excitation energies above their particle-emission thresholds, secondary light-particle emission can affect the mass and energy distributions of the observed fragments. In order to make a realistic comparison of the transition-state model calculations to the experimental results, this secondary light-particle emission has been simulated by using the binary decay option of the LILITA code [33]. The cross sections for the primary mass distribution, obtained from the transition-state model calculations, have been taken as input data. In each fission exit channel, a Gaussian distribution was assumed for the total kinetic energy distribution, with the peak of the distribution obtained using the double spheroid model and the standard deviation taken as 21% of the average value. The total excitation energy was divided between the two fragments assuming equal temperatures.

Comparisons of transition-state model predictions with the experimental cross sections are shown in Fig. 11 for all Z-fragment yields in the range $3\leqslant Z\leqslant 25$. For $3\leqslant Z\leqslant 17$ only the cross sections based on the fully damped yields are shown. For $18\leqslant Z\leqslant 25$ the CF experimental yields are reported. It is worth noting the large shift to lower values that the evaporation process produces in the final fragment-distribution with respect to the primary one. Good overall agreement is found between the experimental results and the transition-state calculations. The calculated fission cross section is 145 mb whereas the corresponding isotropic experimental cross section of 168 ± 30 mb.

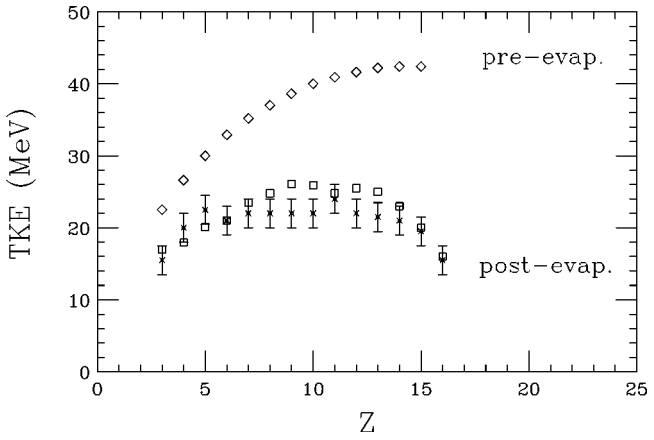

FIG. 12. Average total kinetic energies of the fragments for completely damped processes as a function of their charge Z. Experimental values [crosses with error bars are compared with the fusion-fission model predictions: before evaporation (open diamonds), after correction for evaporation (open squares)].

The calculated and experimental c.m. total kinetic energies of the fragments are compared in Fig. 12. The transition-state model calculations corrected for evaporation are generally in good agreement with the measured kinetic energies. Then the overall agreement suggests that the fully damped yields be ascribed to the fusion-fission process.

VI. LIMITS TO THE ^{59}Cu COMPOUND NUCLEUS FORMATION

The energy dependence of the total fusion cross section can yield important information about the limits of energy and spin that can be sustained by nuclear systems. Fusion cross sections for the ^{35}Cl+^{24}Mg (present work and Ref. [20]), ^{19}F+^{40}Ca [22], and ^{32}S+^{27}Al [22–27] reactions are shown in Fig. 13 as functions of $V_C/E_{\text{c.m.}}$. The Coulomb barrier energy V_C is taken as

$$V_C = 1.44\frac{Z_1 Z_2}{R_B}\left(1-\frac{0.63}{R_B}\right), \tag{6}$$

with

$$R_B = 1.07(A_p^{1/3}+A_t^{1/3})+2.73 \ \ (\text{fm}).$$

A_p and A_t are the projectile and target mass, respectively, in atomic mass units, and R_B is the barrier radius. Each of these reactions populate the ^{59}Cu compound nucleus. The energy dependence of the total reaction cross section, based on optical model calculations for the ^{35}Cl+^{24}Mg system (see caption of Fig. 1), is shown by the long-dashed line in Fig. 13. At energies near and somewhat above the barrier, $V_C/E_{\text{c.m.}} \geq 0.6$ (region I), the fusion cross section is close to the total reaction cross section, except for small departures that result from quasielastic processes. In the range $0.3 \leq V_C/E_{\text{c.m.}} \leq 0.6$ (region II) the fusion cross section initially continues to increase with incident projectile energies, though at a lower rate, and then reaches a saturation point. Competing with fusion, in this energy range, are deep-inelastic processes that are strongly dependent on the entrance-channel mass asymmetry. Region II can be described in terms of the critical distance model [49] or by dynamical trajectories based on friction models. Estimations of the Bass model [50] for disappearance of pocket in the ion-ion potential ($l_{\text{fus}} \approx 38\hbar$), and for the critical angular momentum value ($l_{\text{crit}} = 55\hbar$) rather overestimate the experimental data (see in Fig. 13 the intersection of Bass region II and region III lines).

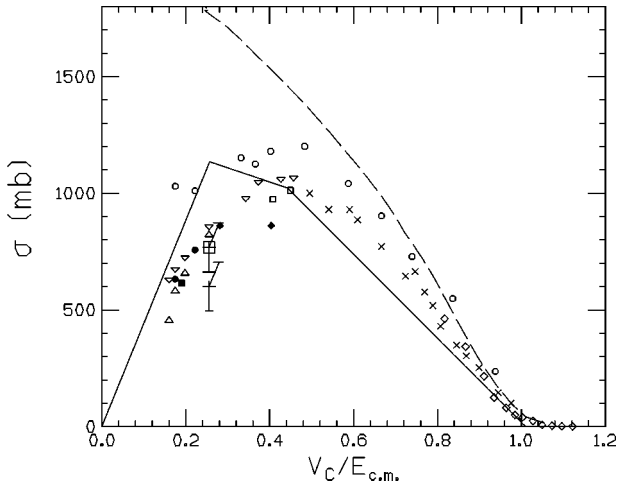

FIG. 13. Fusion excitation functions versus $V_C/E_{\text{c.m.}}$ for different reactions leading to the same compound nucleus ^{69}Cu. Complete fusion component (full circles) and complete plus incomplete (open circles) fusion for the ^{19}F+^{40}Ca reaction [22]. Complete fusion (open triangles [22], full diamonds [23], crosses [24], full square [25], open squares [26]) and complete plus incomplete fusion (inverted open triangles) for the ^{32}S+^{27}Al reaction [27]. Complete fusion-evaporation (diamonds [20], + , present work) and total (+, present work) complete fusion (fusion-evaporation and fission) for the ^{35}Cl+^{24}Mg reaction. The total reaction cross section, calculated with the optical model code PTOLEMY for the reaction ^{35}Cl+^{24}Mg is indicated by the long-dashed line. The three intersecting straight lines represent region I, and Bass estimations for region II and region III, respectively.

At higher energies, $V_C/E_{\text{c.m.}} \leq 0.3$ (region III) incomplete fusion processes can be seen for all three systems, becoming more important with increasing entrance-channel mass asymmetry. In this higher energy region, a strong fission component can be assumed for the ^{35}Cl+^{24}Mg reaction which should be taken into account when determining the complete fusion cross section. However, no fission data are at present available for the two other entrance channels, which makes interesting the question of how this process might influence the fusion cross sections deduced for these systems. On the other hand, although there is some dispersion in the experimental data for the different systems, it is clear that the complete fusion cross sections decrease with increasing energies in region III, suggesting that a common limit is reached for the formation of the ^{59}Cu compound system. Also, this limit appears to be independent of the specific entrance channel. In Fig. 14, the same data are shown in a plot where the excitation energy of the compound nucleus E^* is shown as a function of the critical angular momentum of the compound nucleus, as extracted from the data using the sharp cutoff approximation.

The saturation value found for the critical angular momentum, $J_{\text{cr}} \approx 42 \pm 3.5\hbar$, is consistent with the value at which the fission barrier of the ^{59}Cu compound nucleus vanishes, as

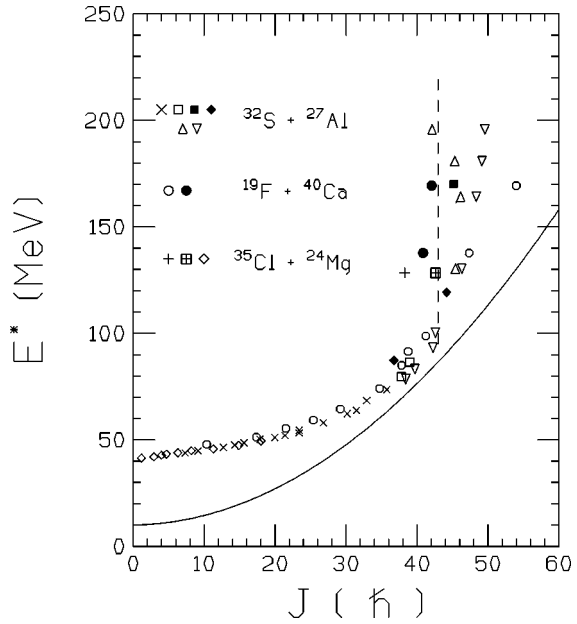

FIG. 14. Excitation energy E^* versus experimental critical angular momenta for the ^{59}Cu CN. The J_{cr} values were extracted from the measured ^{32}S+^{27}Al, ^{19}F+^{40}Ca, and ^{35}Cl+^{24}Mg excitation functions (see text). The symbols represent the same measurements as in Fig. 13. The dashed line represents the disappearance of the fission barrier. The full line is the statistical yrast line given by [56,49]: $E^*=E_{\text{c.m.}}+\Delta Q=[J(J+1)\hbar^2]/2\mathcal{I}$, with $\mathcal{I}=(2/5)R_0A_{CN}^{5/3}$, $\Delta Q=10$ MeV, and $R_0=1.2$ fm.

calculated by the Sierk model [48] and shown as a dashed line in the figure. Similar behavior has been observed for reactions leading to lighter compound nuclei such as ^{40}Ca [51], ^{47}V [8], ^{56}Ni [52,53], and ^{68}Se [54], and is in agreement with the systematics of Beck and Szanto de Toledo [55].

VII. SUMMARY AND CONCLUSIONS

The properties of fusion and competing binary mechanisms have been investigated by the ^{35}Cl+^{24}Mg reaction in the region III at an incident beam energy $E_{\text{lab}}\simeq 282$ MeV, by measuring the inclusive energy spectra and angular distributions of the emitted fragments which have been identified in charge. The ratio of the incomplete fusion to the complete fusion contributions $\sigma_{\text{ICF}}/\sigma_{\text{CF}}\approx 0.05$ to 0.10, has the same value that those found for the ^{32}S+^{27}Al reaction at similar bombarding energies, and therefore consistent with the systematics of Morgenstern *et al.* [10].

In the binary-decay elemental distributions the general inelastic contribution evolves from quasielastic to full energy damping as the charges of fragments are more and more remote from target and projectile Z values.

The partially damped exit channels show both projectilelike and targetlike components, with a decay time much shorter than the rotation time ($0.03\leqslant\tau_1/T\leqslant 0.20$). The total amount of these processes (sum of the fragment contributions up to $Z=16$) can be evaluated to be $\approx$335 mb. The fully damped components of energy spectra can be associated with decay times which are longer than the rotation time, therefore exhibiting their clear long-lived nuclear origin. These components, of constant $d\sigma/d\Theta$ angular distributions, have elemental cross sections and total kinetic energies (corrected for secondary light-particle evaporation) which are well reproduced by the transition state model of Ref. [17]. The total cross section for this component is found to be $\sigma_{FF}\approx 168$ mb. An alternative explanation for these fully damped yields in terms of a dinucleus orbiting mechanism cannot be discounted, although there is no compelling evidence for this alternative based on the observed systematics. The other binary-decay mechanisms which compete strongly with fusion evaporation ($\approx$600 mb), or with fusion followed by evaporation or fission ($\approx$768 mb), are the discussed damped processes ($\approx$335 mb), the incomplete fusion process ($\approx$60 mb), and a quasielastic mechanism, which could not be evaluated with the current experiment. Although with some dispersion, the experimental data clearly indicate a saturation effect in region III which corresponds to a common angular-momentum limitation reached for the formation of the ^{59}Cu compound system.

Based on the present results, it would now be interesting to revisit the previously measured ^{32}S+^{27}Al and ^{19}F+^{40}Ca systems to more clearly establish the compound nucleus origin of the fully energy damped, binary decay yields. This would also help to establish the significance of the observed scatter in total fusion cross sections for the three systems at higher energies.

ACKNOWLEDGMENTS

The authors wish to thank the Post-accelerated Tandem Service, for the kind hospitality and the technical support received during the experiment at the Saclay Laboratories. In particular they would like to mention the help of J. Girard, S. Leotta, and S. Reito of the University of Catania and Istituto Nazionale di Fisica Nucleare di Catania (INFN), respectively, and warmly thank them for their assistance during the experiment.

[1] S.J. Sanders, D.G. Kovar, B.B. Back, C. Beck, B.K. Dichter, D. Henderson, R.V.F. Janssens, J.G. Keller, S. Kaufman, T.F. Wang, B. Wilkins, and F. Videback, Phys. Rev. Lett. **59**, 2856 (1987).

[2] Sl. Cavallaro, G. Prete, and G. Viesti, Phys. Rev. C **41**, 1606 (1990).

[3] C. Beck, B. Djerroud, F. Haas, R.M. Freeman, A. Hachem, B. Heusch, A. Morsad, M. Youlal, Y. Abe, R. Dayras, J.P. Wieleczko, T. Matsuse, and S.M. Lee, Z. Phys. A **343**, 309 (1992); C. Beck, B. Djerroud, B. Heusch, R. Dayras, R.M. Freeman, F. Haas, A. Hachem, J.P. Wieleczko, and Y. Youlal, *ibid.* **334**, 521 (1989); C. Beck, D. Djerroud, F. Haas, R.M. Freeman, A. Hachem, B. Heusch, A. Morsad, M. Vuillet-A-Cilles, and S.J. Sanders, Phys. Rev. C **47**, 2093 (1993); A.

Ray, D. Shapira, J. Gomez del Campo, H.J. Kim, C. Beck, B. Djerroud, B. Heusch, D. Blumenthal, and B. Shivakumar, *ibid.* **44**, 514 (1991).

[4] D. Shapira, R. Novotny, Y.C. Chan, K.A. Erb, J.L.C. Ford, Jr., J.C. Peng, and J.D. Moses, Phys. Lett. **114B**, 111 (1982).

[5] B. Shivakumar, S. Ayik, B.A. Harmon, and D. Shapira, Phys. Rev. C **35**, 1730 (1987).

[6] B. Shivakumar, D. Shapira, P.H. Stelson, S. Ayik, B.A. Harmon, K. Teh, and D.A. Bomley, Phys. Rev. C **37**, 652 (1988).

[7] A.T. Hasan, S.J. Sanders, K.A. Farrar, F.W. Prosser, B.B. Back, R.R. Betts, M. Freer, D.J. Henderson, R.V.F. Janssens, A.H. Wuosmaa, and A. Szanto de Toledo, Phys. Rev. C **49**, 1031 (1994); K.A. Farrar, S.J. Sanders, A.K. Dummer, F.W. Prosser, B.B. Back, I.G. Bearden, R.R. Betts, M.P. Carpenter, B. Crovell, M. Freer, D.J. Henderson, R.V.F. Janssens, T.L. Khoo, T. Lauritzen, Y. Liang, D. Nisius, A.H. Wuosmaa, C. Beck, R.M. Freeman, Sl. Cavallaro, and A. Szanto de Toledo, *ibid.* **54**, 1249 (1996).

[8] R.M. Anjos, N. Added, N. Carlin, L. Fante, Jr., M.C.S. Figueira, R. Matheus, H.R. Schelin, E.M. Szanto, C. Tenreiro, A. Szanto de Toledo, and S.J. Sanders, Phys. Rev. C **48**, R2154 (1993).

[9] C. Beck, Y. Abe, N. Aissaoui, B. Djerroud, and F. Haas, Phys. Rev. C **49**, 2618 (1994); Nucl. Phys. **A583**, 269 (1995).

[10] H. Morgenstern, W. Bohne, W. Galster, K. Grabisch, and A. Kyanowski, Phys. Rev. Lett. **52**, 1104 (1982).

[11] N. Arena, Sb. Cavallaro, S. Feminò , P. Figuera, S. Pirrone, F. Porto, and S. Sambataro, Phys. Rev. C **44**, 1947 (1991).

[12] H. Feldmeier and H. Spangenberger, Nucl. Phys. **A435**, 229 (1985).

[13] P. Fröbrich and S.Y. Xu, Nucl. Phys. **A477**, 143 (1988).

[14] P. Fröbrich and J. Marteen, Z. Phys. A **339**, 171 (1991).

[15] P. Fröbrich and H. Rossner, Z. Phys. A **349**, 99 (1994).

[16] N.D. Mavlitov, P. Fröbrich, and I.I. Gontchar, Z. Phys. A **342**, 195 (1992).

[17] S.J. Sanders, Phys. Rev. C **44**, 2676 (1991).

[18] S. Ayik, D. Shapira, and B. Shivakumar, Phys. Rev. C **38**, 2610 (1988).

[19] S. J. Sanders, *Nuclear Structure and Heavy-ion Reaction Dynamics 1990*, edited by R.R. Betts and J.J. Kolata (IOP, Bristol, 1990), Vol. 109, p. 189.

[20] Sl. Cavallaro, M.L. Sperduto, B. Delaunay, J. Delaunary, A. D'Onofrio, and H. Dumont, Nucl. Phys. **A513**, 174 (1990).

[21] Sl. Cavallaro, C. Beck, E. Berthoumieux, R. Dayras, E. De Filippo, G. Di Natale, B. Djerroud, R.M. Freeman, A. Hachem, F. Haas, B. Heusch, G. Lanzanó, R. Legrain, D. Mahboub, A. Morsad, A. Pagano, E. Pollacco, S.J. Sanders, and M.L. Sperduto, Nucl. Phys. **A583**, 161 (1995).

[22] G. Rosner, J. Pochodzalla, B. Heck, G. Hlawatsch, A. Miczaika, H.J. Rabe, R. Butsch, B. Kolb, and B. Sedelmeyer, Phys. Lett. **150B**, 87 (1985).

[23] F. Pühlhofer, W.F.W. Schneider, F. Busch, J. Barrette, P. Braun-Muzinger, C.K. Gelbke, and H.E. Wegner, Phys. Rev. C **16**, 1010 (1977).

[24] H.H. Gutbrod, W.G. Winn, and M. Blann, Nucl. Phys. **A213**, 267 (1973).

[25] R.L. Kozub, N.H. Lu, J.M. Miller, D. Logan, T.W. Lebiak, and L. Kowalski, Phys. Rev. C **11**, 1497 (1975).

[26] F. Porto, S. Sambataro, K. Kusterer, Liu Ken Pao, G. Doukellis, and H.L. Harney, Nucl. Phys. **A357**, 237 (1981).

[27] G. Doukellis, G. Klawatsch, B. Kolb, A. Miczaika, G. Rosner, and B. Sedelmeyer, Nucl. Phys. **A485**, 369 (1988).

[28] D. Mahboub, Ph.D. thesis, Université Louis Pasteur Strasbourg, Report 2482 CNR-96-36 (unpublished).

[29] R. Nouicer, C. Beck, D. Mahboub, T. Matsuse, B. Djerroud, R.M. Freeman, A. Hachem, Sl. Cavallaro, E. De Filippo, G. Lanzanó, A. Pagano, M.L. Sperduto, R. Dayras, E. Berthoumieux, R. Legrain, and E. Pollacco, Z. Phys. A **356**, 5 (1996).

[30] C. Beck, D. Mahboub, R. Nouicer, T. Matsuse, B. Djerroud, R.M. Freeman, F. Haas, A. Hachem, A. Morsad, M. Youlal, S.J. Sanders, R. Dayras, J.P. Wieleczko, E. Berthoumieux, R. Legrain, E. Pollacco, Sl. Cavallaro, E. De Filippo, G. Lanzanó, A. Pagano, and M.L. Sperduto, Phys. Rev. C **54**, 227 (1996).

[31] J.L. Ferrero, J.C. Pacheco, A. Baeza, J.M. Barrigon, B. Bilwes, R. Bilwes, and N. Vinh Mau, Nucl. Phys. **A514**, 367 (1990).

[32] S.B. Kaufman, E.P. Steinberg, B.D. Wilkins, J. Unik, A.J. Gorski, and M.J. Fluss, Nucl. Instrum. Methods **115**, 47 (1974).

[33] J. Gomez del Campo and R.G. Stokstad, Oak Ridge National Laboratory Report No. ORNL/TM-7295, 1981; J. Gomez del Campo, R.G. Stokstad, J.A. Biggerstaff, R. Dayras, A.H. Snell, and P.H. Stelson, Phys. Rev. C **19**, 2170 (1979).

[34] F. Pühlhofer, Nucl. Phys. **A280**, 267 (1977).

[35] Sl. Cavallaro, Yin Shu Zhi, G. Prete, and G. Viesti, Phys. Rev. C **40**, 98 (1989).

[36] G. Viesti, B. Fornal, D. Fabris, K. Hagel, J.B. Natowitz, G. Nebbia, G. Prete, and F. Trotti, Phys. Rev. C **38**, 2640 (1988).

[37] G. La Rana, R. Moro, A. Brondi, P. Cuzzocrea, A. D'Onofrio, E. Perillo, M. Romano, F. Terrasi, E. Vardaci, and H. Dumont, Phys. Rev. C **37**, 1920 (1988).

[38] J.R. Huizenga, A.N. Behkami, I.M. Govil, W.U. Schroder, and J. Toke, Phys. Rev. C **40**, 668 (1989).

[39] N.G. Nicolis and D.G. Sarantites, Phys. Rev. C **40**, 2422 (1989).

[40] G. La Rana, R. Moro, A. Brondi, P. Cuzzocrea, A. D'onofrio, E. Perillo, M. Romano, and F. Terrasi, Phys. Rev. C **40**, 2425 (1989).

[41] J.M. Alexander, M.T. Magda, and S. Landowne, Phys. Rev. C **42**, 1092 (1990).

[42] K. Kildir, G. La Rana, R. Moro, A. Brondi, E. Vardaci, A. D'onofrio, D. Fessas, E. Perillo, V. Roca, M. Romano, F. Terrasi, G. Nebbia, G. Viesti, and G. Prete, Phys. Rev. C **51**, 1873 (1995).

[43] K. Dietrich, K. Pomorski, and J. Richert, Z. Phys. A **351**, 397 (1995).

[44] C.K. Gelbke, C. Olmer, M. Buenerd, D.L. Hendrie, J. Mahoney, M.C. Mermaz, and D.K. Scott, Phys. Rep. **42**, 311 (1978).

[45] M.H. Simbel and A.Y. Abul Magd, Z. Phys. A **294**, 277 (1980).

[46] L. Moretto, Nucl. Phys. **A247**, 211 (1975).

[47] R.J. Charity, M.A. MacMahan, G.J. Wozniak, R.J. McDonald, L.G. Moretto, D.G. Sarantites, L.G. Sobotka, C. Guarino, A. Pantaleo, L. Fiore, A. Gobbi, and H. Hildebrand, Nucl. Phys. **A483**, 371 (1988).

[48] A.J. Sierk, Phys. Rev. C **33**, 2039 (1986).

[49] S.M. Lee, T. Matsuse, and A. Arima, Phys. Rev. Lett. **45**, 165 (1980); T. Matsuse, S. M. Lee, Y.H. Pu, K.Y. Nakagawa, C. Beck, and T. Nakagawa, *International Symposium NIKKO'91*, Nikko, Japan, 1991 (unpublished); T. Matsuse, in *Proceedings of the Tsukuba International Symposium on Heavy Ion Fusion*

Reactions, edited by K. Furuno and T. Kishimoto, Tsukuba, Japan, 1984 (unpublished), p. 113; T. Matsuse, C. Beck, R. Nouicer, and D. Mahboub, Phys. Rev. C **55**, 1380 (1997).

[50] R. Bass, *Nuclear Reactions with Heavy Ions* (Springer-Verlag, Berlin, 1980), p. 327.

[51] M.F. Vineyard, J.F. Mateja, C. Beck, S.E. Atencio, L.C. Dennis, A.D. Frawley, D.J. Henderson, R.V.F. Janssens, K.W. Kemper, D.G. Kovar, C.F. Maguire, S.J. Paladino, F.W. Prosser, G.S.F. Stephans, M.A. Tiede, B.D. Wilkins, and R.A. Zingarelli, Phys. Rev. C **47**, 2374 (1993).

[52] S.J. Sanders, D.G. Kovar, B.B. Back, C. Beck, D.J. Henderson, R.V.F. Janssens, T.F. Wang, and B.D. Wilkins, Phys. Rev. C **40**, 2091 (1989).

[53] C. Beck, D.G. Kovar, S.J. Sanders, B.D. Wilkins, D.J. Henderson, R.V.F. Janssens, W.C. Ma, M.F. Vineyard, T.F. Wang, C.F. Maguire, F.W. Prosser, and G. Rosner, Phys. Rev. C **39**, 2202 (1989); M.F. Vineyard, J.S. Bauer, C.H. Gosdin, R.S. Trotter, D.G. Kovar, C. Beck, D.J. Henderson, R.V.F. Janssens, B.D. Wilkins, G. Rosner, P. Chowdhury, H. Ikezoe, W. Kuhn, J.J. Kolata, J.D. Hinnefeld, C.F. Maguire, J.F. Mateja, F.W. Prosser, and G.S.F. Stephans, *ibid.* **41**, 1005 (1990).

[54] M.F. Vineyard, J.S. Bauer, J.F. Crum, C.D. Gosdin, R.S. Trotter, D.G. Kovar, C. Beck, D.J. Henderson, R.V.F. Janssens, B.D. Wilkins, C.F. Maguire, J.F. Mateja, F.W. Prosser, and G.S.F. Stephans, Phys. Rev. C **45**, 1784 (1992).

[55] C. Beck and Szanto de Toledo, Phys. Rev. C **53**, 1989 (1996).

[56] S. Harar, in *Nuclear Molecular Phenomena*, edited by N. Cindro (North-Holland, Amsterdam, 1978), p. 329.